

Unraveling oxygen vacancy changes of WO_3 photoanodes for promoting oxygen evolution reaction

Lianglin Yan ^{a,b}, Guojun Dong ^{b,*}, Xiaojuan Huang ^b, Yun Zhang ^{a,*}, Yingpu Bi ^{b,*}

^a Gansu Key Laboratory for Environmental Pollution Prediction and Control, College of Earth and Environmental Sciences, Lanzhou University, Lanzhou 730000, China

^b State Key Laboratory for Oxo Synthesis & Selective Oxidation, National Engineering Research Center of Fine Petrochemical Intermediates, Lanzhou Institute of Chemical Physics, CAS, Lanzhou 730000, China



ARTICLE INFO

Keywords:

Oxygen vacancy
Self-healing
Water oxidation
Photoelectrocatalysis
 WO_3 photoanode

ABSTRACT

Oxygen vacancy (V_O) on semiconductor photoanode plays an important role in enhancing photoelectrochemical water oxidation performances. Nonetheless, there is still a lack of definitive elucidation regarding the structural changes and their impact on charge transport during the oxygen evolution reaction (OER). Herein, oxygen vacancies were rationally introduced on WO_3 nanoflake photoanodes via Ar-plasma engraving, resulting in a threefold increase in the photocurrent density of 2.76 mA cm^{-2} at $1.23 \text{ V}_{\text{RHE}}$ under AM 1.5 G solar irradiation compared to the pristine WO_3 photoanode. Comprehensive experiments and theoretical calculations reveal that the self-healing process of surface oxygen vacancies on WO_3 photoanodes should be more easily achieved by capturing oxygen atoms from adsorbed H_2O molecules. However, some survived oxygen vacancies in the subsurface could effectively increase the charge carrier density and provide the additional driving force to accelerate the interfacial charge transport, leading to enhanced photoelectrochemical (PEC) activities. More importantly, the oxygen vacancy self-healing on metal-oxide semiconductors is a universal phenomenon, which might bring new insights for design and construction of highly efficient photoanodes for PEC water oxidation.

1. Introduction

Photoelectrochemical (PEC) water splitting is a promising method for converting abundant solar-energy into clean and sustainable hydrogen fuels [1,2]. Up to now, various oxide semiconductor materials, including TiO_2 , Fe_2O_3 , WO_3 and BiVO_4 , have been considered as promising photoanode candidates due to their suitable band positions, low fabrication costs and non-toxic properties [3–7]. In order to achieve high-efficient PEC water splitting activities, over the past few decades, strategies such as morphology control, heterojunction construction, and co-catalyst modification have been widely employed to enhance the photogenerated charge separation and transport abilities [8–11]. For examples, one-dimensional nanostructures were used to improve the directional charge transport of Fe_2O_3 or TiO_2 [12,13]. The incorporation of FeOOH cocatalysts on BiVO_4 surface could improve the surface charge separation and utilization efficiency for PEC water oxidation [14]. Despite the progress have achieved in photoanode material design, the attained photocurrent density and photo-conversion efficiency of existing semiconductor photoanodes still fail to meet the minimum requirements for commercial PEC applications due to the intrinsic

limitations in charge carrier mobility and slow oxygen evolution kinetics.

In recent years, oxygen vacancies engineering has been demonstrated to be an efficient approach for boosting PEC water oxidation activities, which could modulate the local electronic structure of semiconductor photoanode materials to facilitate charge transfer and separation while altering the surface atomic coordination environment, thereby enhancing the oxygen evolution reactivity at the electrode/electrolyte interface [15–18]. For instance, Li et al. proved that the construction of oxygen vacancies on the WO_3 photoanode promoted photogenerated carrier transfer ability [19]. Lee and co-workers displayed that the separation efficiency of electron-hole pairs could be significantly enhanced after the formation of oxygen vacancies [20]. Xu et al. reported that the surface oxygen defects were contributing to water molecule adsorption and activation, thus accelerating the water oxidation reaction [21]. However, most studies have focused on aspects such as the fabrication methods of oxygen vacancies, as well as the relationship between V_O concentration and PEC performances [22–24]. There is little research has addressed the specific changes in oxygen vacancies on the photoanode materials during the OER process and the

* Corresponding authors.

E-mail addresses: dongguojun@licp.ac.cn (G. Dong), zhangyun@lzu.edu.cn (Y. Zhang), yingpubi@licp.ac.cn (Y. Bi).

corresponding mechanisms affecting photogenerated charge transfer efficiency.

Herein, the oxygen vacancies were controllably constructed on WO_3 nanoflake photoanode using a simple Ar-plasma engraving method, leading to a significantly improvement in PEC water oxidation activity. After 60 s of treatment, the engraved WO_3 ($\text{WO}_3\text{-V}_0$) displays an exceptional photocurrent density of 2.76 mA cm^{-2} at 1.23 V vs. RHE under simulated solar irradiation (AM 1.5 G, 100 mW cm^{-2}), which is approximately 3 times higher than that of pristine WO_3 samples. Furthermore, a noteworthy lattice self-healing phenomenon of surface oxygen vacancies was observed through X-ray photoelectron spectroscopy (XPS) upon the adsorption of H_2O on the $\text{WO}_3\text{-V}_0$. When combined with the improved PEC performance of the $\text{WO}_3\text{-V}_0$ photoanode, it can be reasonably conjectured that the accelerated interface charge transport is driven by the subsurface oxygen vacancies. Additionally, the related Density Functional Theory (DFT) calculations further confirmed the lattice self-repairing of surface oxygen vacancies and the favorable water oxidation activities of subsurface oxygen vacancies. These findings present a novel understanding into the changes of oxygen vacancies on semiconductor photoanodes and their impact on the water oxidation performances.

2. Experimental section

2.1. Preparation of WO_3 and $\text{WO}_3\text{-V}_0$ photoanode

The nanoflake WO_3 photoanode was obtained based on the previous report [25]. Briefly, a seed layer solution was initially spin-coated onto fluorine-doped tin oxide (FTO) substrates and subsequently annealed at 500°C for 2 h in ambient air. Subsequently, a mixture comprising 6 mL of H_2WO_4 solution (0.15 M), 0.04 g of urea, 0.04 g of oxalic acid, 25 mL of acetonitrile, and 1 mL of HCl (6 M) was prepared and used for the hydrothermal growth of WO_3 nanoflakes in a 50 mL Teflon-lined autoclave at 180°C for 2 h. The pristine WO_3 photoanode was then obtained after annealing at 500°C for 2 h.

The $\text{WO}_3\text{-V}_0$ nanoflakes were produced using a simple Ar-plasma engraving process. The prepared WO_3 photoanode was engraved at 6.8 W for duration of 30 s, 60 s, 90 s, and 180 s, resulting in the corresponding photoanodes named $\text{WO}_3\text{-V}_0\text{-30 s}$, $\text{WO}_3\text{-V}_0$, $\text{WO}_3\text{-V}_0\text{-90 s}$ and $\text{WO}_3\text{-V}_0\text{-180 s}$, respectively.

The seed layer solution is prepared by adding 2.5 g H_2WO_4 and 1 g polyvinyl alcohol (PVA) into 34 mL H_2O_2 (30%). The 0.15 M H_2WO_4 solution was prepared by dissolving 3.75 g H_2WO_4 into mixed solution (33 mL H_2O and 17 mL H_2O_2) at 95°C . The above solution was diluted using deionized water to 100 mL to obtain the 0.15 M H_2WO_4 solution.

2.2. Characterization

The sample morphology and elemental mapping were obtained by ultrahigh resolution field emission scanning electron microscope (SEM, SU8020; HITACHI) and field emission transmission electron microscope (TEM, TECNAI G² TF20; FEI), respectively. The crystalline structure of the samples was identified by polycrystalline powder X-ray diffractometer (XRD, Smartlab-SE; Rigaku Corporation). The surface chemical valence states and valence band spectra were determined by X-ray photoelectron spectroscopy (XPS, ESCALAB 250Xi; ThermoFisher Scientific). Raman spectra were obtained by confocal microprobe Raman spectroscopy (LabRAM HR Evolution, HORIBA Jobin Yvon S.A.S.). UV-visible diffuse reflectance spectra were performed on an ultraviolet-visible spectrophotometer (UV-2550, Shimadzu) by using BaSO_4 as the reference. The photoluminescence (PL) spectra were attained on fluorescence spectrophotometer (F-7000, Hitachi) with a laser excitation of 280 nm. The plasma engraving treatment was carried out by a plasma cleaner (PDC-36 G, Hefei Kejing Materials Technology Co., Ltd.). Scanning photoelectrochemical microscopy (SPECM, VersaSCAN; AMETEK) measurements were carried out on a simulated sunlight (AM

1.5 G) and SPECM platform in a standard three-electrode system. The SPECM electrolyte is a mixture of 5 mM $\text{K}_3[\text{Fe}(\text{CN})_6]$, 5 mM $\text{K}_4[\text{Fe}(\text{CN})_6]$ and 0.1 M KCl.

2.3. Photoelectrochemical measurements

The photoelectrochemical properties were gained access to an electrochemical analyzer (CHI660D) in a standard three-electrode system, in which the WO_3 photoanode was working electrode, the Pt foil was the counter electrode and the Ag/AgCl was the reference electrode. The 0.1 M phosphate buffer solution (PBS, pH = 7) was applied as electrolyte. The optical-fiber Light source (FX300, Beijing Perfect Light Technology Co., Ltd) with an AM 1.5 G filter was applied as illumination source to simulate sunlight. The light intensity was calibrated to 100 mW cm^{-2} by Dual Channel Bench Power and Energy Meters Console (PM320E, THORLABS) equipped with Standard thermal power probe (S310C, THORLABS). Linear-sweep voltammograms (LSV) curves were measured by scanning potential from -0.2 to 1.0 V (vs. Ag/AgCl) with a scan rate of 10 mV s^{-1} and the applied potentials could be converted into reversible hydrogen electrode (RHE): $E_{\text{RHE}} = E_{\text{Ag/AgCl}} + 0.0591 \times \text{pH} + 0.197$. Where E_{RHE} refers to the converted potential versus RHE, $E_{\text{Ag/AgCl}}$ is the obtained potential versus Ag/AgCl. The evolution of H_2 and O_2 was studied in a 0.1 M PBS electrolyte at $1.23 \text{ V}_{\text{RHE}}$ under AM 1.5 G illumination (100 mW cm^{-2}) by an online gas analysis system (Labsolar 6 A, Beijing Perfect light Technology Co. Ltd.) and a gas chromatograph (GC 7890 A, Agilent Technologies).

2.4. DFT calculation

All calculations were carried out with Cambridge Sequential Total Energy Package (CASTEP) code based on density functional theory [26, 27]. The Generalized Gradient Approximation (GGA) with the Perdew-Burke-Ernzerhof (PBE) function was applied to describe the exchange-correlation effects [28,29]. The pseudo-hydrogen saturated WO_3 (010) surface was selected for Geometry optimization and Energy calculations based on XRD results of prepared WO_3 in experiment. A plane wave cutoff energy of 500 eV and a Monkhorst-Pack grid of $2 \times 1 \times 1$ were used, in which the self-consistent convergence accuracy is $1.0 \times 10^{-5} \text{ eV/atom}$, the convergence criterion for the maximal force on atoms is $0.05 \text{ eV}/\text{\AA}$. A 15 Å vacuum region is constructed in the z-direction to minimize the interaction between periodic images. The active site was discovered through the exploration of DFT energy for the water oxidation process on the WO_3 -sub- V_0 model. The Gibbs free energy (G) for each process is calculated using the equation: $G = E + E_{\text{ZPE}} - TS$, where E, E_{ZPE} , and S represent the DFT energy, zero-point energy, and entropy at 298 K, respectively.

3. Results and discussion

3.1. Morphology and structure characterization

The schematic illustration for the synthetic process of all photoanodes is shown in Fig. S1. The WO_3 nanoflake arrays were firstly prepared on a fluorine-doped tin oxide (FTO) conductive substrate by a seed crystal-induced method, which was subsequently engraved by Ar-plasma for constructing oxygen vacancies on WO_3 to obtain $\text{WO}_3\text{-V}_0$. Fig. 1A and B depict typical scanning electron microscope (SEM) images of $\text{WO}_3\text{-V}_0$, the well-defined nanoflakes grow vertically aligned on the FTO, and the film thickness of the photoanode is about 3.1 μm. As observed in the transmission electron microscopy (TEM) image in Fig. 1C, a multitude of pores permeate the nanoflake structure, which is advantageous for the oxygen evolution reaction. Evidently, $\text{WO}_3\text{-V}_0$ maintains similar morphological and structure features as pristine WO_3 photoanode (Fig. S2). To gain further insights into the influence of Ar-plasma treatment on the WO_3 structure, high-resolution TEM (HRTEM) was employed. In contrast to the pristine WO_3 , which exhibits

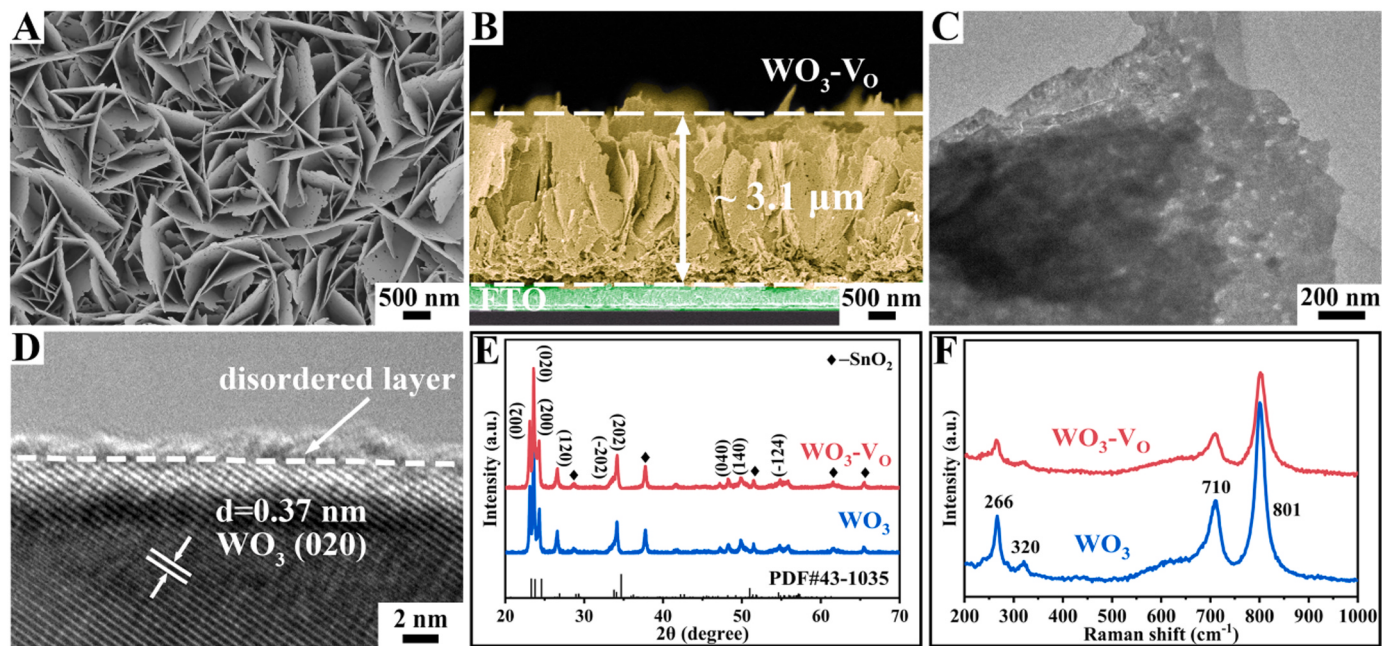


Fig. 1. SEM images of (A) top-view and (B) cross-view of $\text{WO}_3\text{-V}_\text{O}$ photoanodes. (C) TEM and (D) HRTEM images of $\text{WO}_3\text{-V}_\text{O}$ photoanodes. (E) XRD patterns and (F) Raman spectra of pristine WO_3 and $\text{WO}_3\text{-V}_\text{O}$.

well-defined crystal boundaries (Fig. S2D), $\text{WO}_3\text{-V}_\text{O}$ displays a disordered layer on its surface with an approximate thickness of 2.0 nm in Fig. 1D. This disordered layer may be attributed to the formation of numerous oxygen vacancies [30,31]. Additionally, as demonstrated in Fig. S3, elemental mapping indicated that both W and O elements maintain a uniform distribution across the entire region after Ar-plasma bombardment. In addition, the X-ray diffraction (XRD) and Raman spectroscopy were used to analysis the phase characteristics of the $\text{WO}_3\text{-V}_\text{O}$ photoanode. As shown in Fig. 1E, due to the strong penetration depth of X-rays, there is no significant difference between the diffraction peaks of WO_3 and $\text{WO}_3\text{-V}_\text{O}$, which can be indexed as the monoclinic phase of WO_3 (JCPDS no. 43–1035) [32]. However, it is evident that the peak intensities of O-W-O bending (266 and 320 cm^{-1}) and stretching (710 and 801 cm^{-1}) mode in $\text{WO}_3\text{-V}_\text{O}$ have significantly decreased compared with pure WO_3 in Raman spectra (Fig. 1F), implying the establishment of oxygen vacancies on WO_3 surface [33,34]. XRD and Raman results for photoanodes at different engraving times are also presented in the supplementary information (Fig. S4). Furthermore, the UV-Vis diffuse reflectance spectra in Fig. S5 also could demonstrate the existence of abundant oxygen vacancies in $\text{WO}_3\text{-V}_\text{O}$ photoanodes owing to the additional tail-like absorption at higher wavelength ($> 450\text{ nm}$) [35]. The above analyses indicate that V_O modified WO_3 photoanode have been successfully constructed by Ar-plasma engraving treatment, and the concentration of oxygen vacancies has gradually increased with increasing engraving time.

3.2. Photoelectrochemical activity

The PEC water splitting performances of $\text{WO}_3\text{-V}_\text{O}$ photoanodes were evaluated in 0.1 M phosphate buffer electrolyte ($\text{pH}=7$) under AM 1.5 G solar irradiation (100 mW cm^{-2}) using a standard three-electrode system. Other photoanodes have also been examined under the same conditions for PEC activity comparison. Fig. 2 A presents the linear sweep voltammetry (LSV) curves, and it is clear that the $\text{WO}_3\text{-V}_\text{O}$ exhibits a photocurrent density of 2.76 mA cm^{-2} at $1.23\text{ V}_{\text{RHE}}$, which is higher than that of the pristine WO_3 photoanode (0.94 mA cm^{-2}). Furthermore, Fig. S6 presents a comparison of photocurrents for WO_3 photoanodes at different engraving times. These results demonstrate that the creation of appropriate number of oxygen vacancies on WO_3 could

significantly improve its photocurrent density. Moreover, the photoelectric conversion abilities of the prepared photoanodes were assessed by incident photo-to-current conversion efficiency (IPCE). As depicted in Fig. 2B, the IPCE exhibits a similar distribution compared to the I-V features, with $\text{WO}_3\text{-V}_\text{O}$ achieving the highest value of 81.6% at 350 nm . To examine the interfacial water oxidation kinetics, the electrochemical impedance spectroscopy (EIS) was carried out and is presented in Fig. 2 C, it can be seen that $\text{WO}_3\text{-V}_\text{O}$ possesses a smaller arc radius than WO_3 , implying that the interfacial charge separation abilities of WO_3 could be remarkably increased after the introduction of oxygen vacancies [36,37]. Additionally, the surface charge separation efficiency was calculated under the condition using $0.1\text{ M Na}_2\text{SO}_3$ as a hole scavenger (Figs. 2D and S7). The introduction of oxygen vacancies can improve the surface charge separation efficiency from 37.7% (WO_3) to 91.2% ($\text{WO}_3\text{-V}_\text{O}$) at $1.23\text{ V}_{\text{RHE}}$. In addition, Mott-Schottky curves are presented in Fig. 2E, indicating that the carrier density ($N_\text{d}: 3.53 \times 10^{19}\text{ cm}^{-3}$) of $\text{WO}_3\text{-V}_\text{O}$ is higher than that of WO_3 ($N_\text{d}: 1.8 \times 10^{20}\text{ cm}^{-3}$), which is beneficial for accelerating charge transport due to its high conductivity [38,39]. An online gas chromatography (GC) was employed to detect the amounts of hydrogen and oxygen generated from PEC water splitting over $\text{WO}_3\text{-V}_\text{O}$ photoanodes, as shown in Fig. 2 F, the volumes of H_2 and O_2 generated after 60 min of irradiation were $19.39\text{ }\mu\text{mol}$ (FE: 92.4%) and $9.26\text{ }\mu\text{mol}$ (FE: 88.3%), respectively, indicating a stoichiometric ratio of 2: 1 from the water splitting.

The electrochemical performances of photoanodes were also evaluated in same electrolyte (Fig. S8), the $\text{WO}_3\text{-V}_\text{O}$ displays a higher current density than that of WO_3 under the equal bias voltage, demonstrating the superior OER activity of WO_3 photoanode after Ar-plasma treatment [40]. More importantly, scanning photoelectrochemical microscopy (SPECM) was performed to explore the surface photoactive properties. As shown in Fig. 2 G and H, a relatively low photocurrent was observed in the WO_3 regions under light illumination, while the photocurrent drastically increased when the SPECM probe was scanning to the $\text{WO}_3\text{-V}_\text{O}$ regions, illustrating the enhanced PEC water oxidation ability of WO_3 with oxygen vacancies. Besides, the recombination ratios of photogenerated electrons and holes could be effectively reduced through the construction of oxygen vacancies, as indicated by the lower PL peak of $\text{WO}_3\text{-V}_\text{O}$ photoanode (Fig. 2I) [41]. Therefore, the introduction of oxygen vacancies on the WO_3 photoanode could noticeably

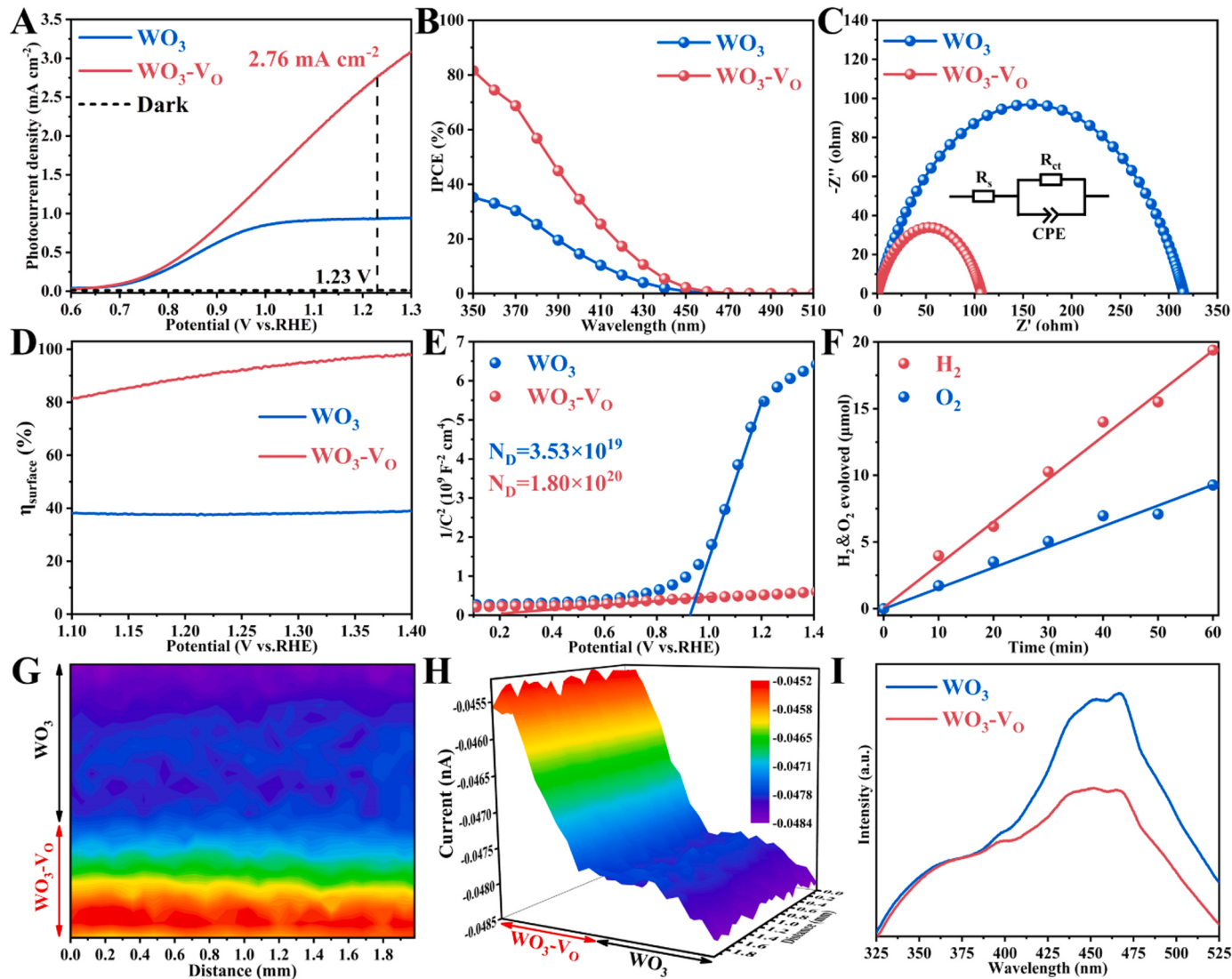


Fig. 2. (A) Linear-sweep voltammograms (LSV); (B) Incident photon to current conversion efficiency (IPCE); (C) Electrochemical impedance spectroscopy (EIS); (D) Charge transfer efficiencies (η_{trans}); (E) Mott-Schottky plots for WO_3 and WO_3 - Vo photoanodes; (F) H_2 and O_2 evolution of WO_3 - Vo measured at 1.23 V vs. RHE. (G) Top and (H) side view of SPECM surface photocurrents under light irradiation. (I) PL spectra for WO_3 and WO_3 - Vo photoanodes.

promote photogenerated charge separation and utilization efficiency, resulting in promoted PEC water splitting activities.

3.3. Oxygen vacancy structure and mechanism

To further investigate the impact of oxygen vacancy on enhanced PEC performance, we employed X-ray photoelectron spectroscopy (XPS) to examine the chemical states of WO_3 and WO_3 - Vo before and after the adsorption of H_2O . In pristine WO_3 (Fig. S10A and B), the W 4 f spectrum of WO_3 could be deconvoluted into W^{6+} (at 35.6 eV and 37.8 eV) and W^{5+} (at 34.4 eV and 36.6 eV) [42], and O 1 s peaks could be indexed to the lattice oxygen (530.3 eV , O_{l}), oxygen vacancy (531.3 eV , O_{v}) and absorbed water (532.5 eV , $\text{O}_{\text{H}_2\text{O}}$), respectively [43]. Following Ar-plasma engraving treatment (Fig. 3A and B), not only the + 5 valence peak ratio enlarge, but a distinct + 4 valence peak also emerged in the W 4 f spectrum. Regarding the O 1 s peak, the fitted area of O_{v} exhibited a noticeable increase, indicating the creation of a substantial amount of oxygen vacancies on WO_3 photoanode [44]. More notably, after H_2O adsorption (Fig. 3C and D), both W^{5+} and O_{v} in WO_3 - Vo showed a reduction in peak area, while the $\text{O}_{\text{H}_2\text{O}}$ peak area significantly increased. This demonstrates the successful adsorption of H_2O molecules on

WO_3 - Vo and a subsequent decrease in the quantity of oxygen vacancies. Importantly, the peak areas of W^{5+} and O_{v} in H_2O -adsorbed WO_3 - Vo are still larger than those in the pristine WO_3 , suggesting that surface oxygen vacancies may be repaired by the adsorbed H_2O , and the partially detected oxygen vacancies may survive in the subsurface of WO_3 [45]. For comparison, XPS analysis of H_2O -adsorbed WO_3 sample (Fig. S10C and D) showed that the peak shapes and area ratios of W 4 f and O 1 s remained consistent before and after H_2O adsorption, confirming that the observed lattice repair is attributed to the self-healing of surface oxygen vacancies triggered by adsorbed H_2O . In Fig. 3E, WO_3 - Vo exhibited a stronger W 5d-driven peak near the Fermi level than WO_3 , indicating the generation of numerous oxygen vacancies in WO_3 after engraving. This peak diminished in the WO_3 - Vo sample after H_2O adsorption, further identifying the lattice self-repairing caused by H_2O molecular on WO_3 - Vo surface [46]. HRTEM analysis (Fig. S11) further verified this self-healing phenomenon, which is more pronounced in XPS results of excessively engraved WO_3 sample (Fig. S12). Additionally, the intensity variation of Raman spectra (Fig. S13) also supported this phenomenon of surface oxygen vacancies in WO_3 - Vo upon water adsorption. Consequently, as being illustrated in Fig. 3F, we can reasonably conclude that lattice self-repairing occurs on the surface

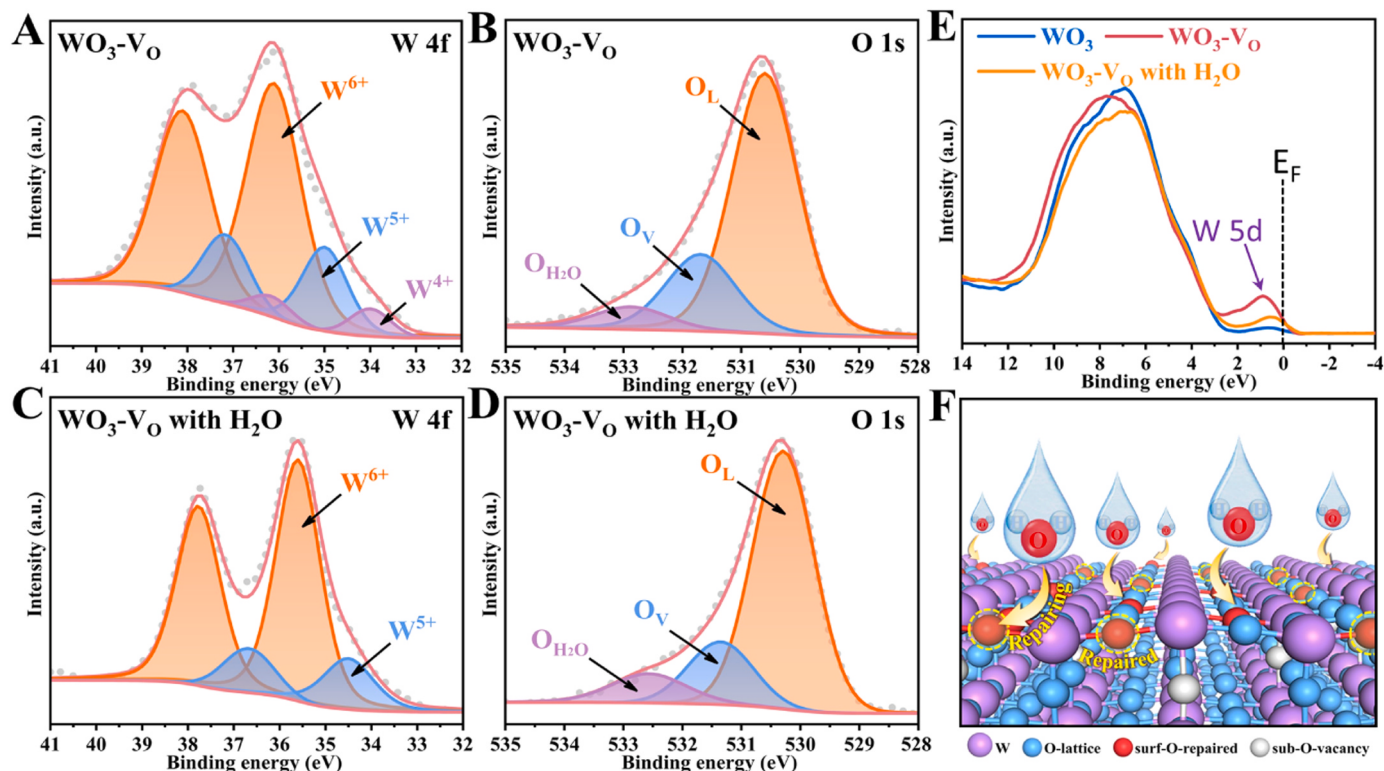


Fig. 3. The high-resolution XPS spectra for (A) W 4 f spectra and (B) O 1 s spectra of WO₃-V_O; (C) W 4 f spectra and (D) O 1 s spectra of WO₃-V_O after H₂O adsorption; (E) The valence band spectra for WO₃, WO₃-V_O, and H₂O absorbed WO₃-V_O; (F) Schematic illustration of lattice self-repairing for surface oxygen vacancies in WO₃-V_O.

oxygen vacancies of the WO₃-V_O photoanode during water oxidation reaction. The partially detected oxygen vacancies may persist in the subsurface of WO₃-V_O and play a crucial role in promoting interfacial charge transfer. To validate the universal variation styles and roles of photoanode oxygen vacancies in the process of OER, the PEC performances and corresponding XPS analyses of Ar-plasma engraved TiO₂ were detected and shown in Figs. S15 and 16. The detailed discussions are described in supporting information, it is not difficult to observe that they exhibit highly similar PEC characteristics and oxygen vacancy variations to WO₃ photoanode, which strongly supports the lattice self-repairing of surface oxygen vacancies on the photoanode and the role of subsurface oxygen vacancies in enhancing water oxidation activities.

Moreover, density functional theory (DFT) calculations have also been performed to investigate the electron properties and water oxidation process of WO₃ with subsurface oxygen vacancies (WO₃-sub-V_O). As illustrated in Fig. S17, compared with the pure WO₃, the partial density of states (pDOS) of WO₃-sub-V_O shows a novel defect energy level originating from W-d states within its band gap, suggesting that the formation of subsurface vacancies in WO₃ photoanode has the potential to enhance its conductivity, thereby facilitating interface charge transfer [47]. Meanwhile, the introduced impurity states could reduce the filling of antibonding states to facilitate H₂O oxidation [48]. The above theoretical analysis is consistent with the experimental results on PEC performances. In addition, based on a previous study on the pathway of the oxygen evolution reaction (OER), the adsorption of consecutive intermediate species (OH, O, OOH) on the catalyst surface (*) can be described by the four equations shown in Tab. S1, and the overall OER mechanism is also presented on the surface of the WO₃ semiconductor in Fig. S17C [49,50]. In order to examine the possible OER active site, the four W positions were utilized to absorb intermediate species on the WO₃-sub-V_O model by comparing the DFT total energy (Fig. S18). From the summarized energy in Tab. S2, it is obvious that the first W position

is most likely the OER catalytic active site. Therefore, the first W position was also selected to calculate the Gibbs free energy (ΔG) of OER pathway in other models (pure WO₃ and WO₃-surf-V_O).

The optimized structures and ΔG of intermediate species in OER pathway for WO₃, WO₃-sub-V_O and WO₃-surf-V_O at the equilibrium potential (U = 0 V) were shown in Fig. 4 A and B, respectively. It is obvious that the ΔG_{*OH} of all samples show a downhill trend, implying that H₂O molecular can be spontaneously adsorbed on the WO₃ (010) surface with or without oxygen vacancies. More interestingly, the surface vacancies of WO₃ could be filled with the oxygen from adsorbed H₂O to form a stable surface configuration, thus the corresponding value of ΔG_{*O} becomes more negative in WO₃-surf-V_O models. These results indicate that the surface vacancies of WO₃ are most likely to be self-repaired in H₂O oxidation reaction, which is consistent with the above mentioned XPS and HRTEM results. From the OER reaction steps (Fig. 4B), the rate-determining step for all WO₃ samples is the transition from *O to *OOH, and the minimum ΔG_{*OOH} occurs on WO₃-sub-V_O model, implying that subsurface oxygen vacancies play the most crucial role in facilitating OER reactions. Therefore, under the solar irradiation, surface-accumulated photogenerated holes will be rapidly transferred and participated in water oxidation reactions owing to the strong driven force from sub-surface vacancies. Based on the above experimental analyses and theoretical calculations, it can be concluded that the surface oxygen vacancies in WO₃-V_O repair its lattice by capturing the O atoms from adsorbed H₂O molecules during the water oxidation reaction, and the enhanced interfacial charge transport abilities are mainly attributed to the subsurface oxygen vacancies.

4. Conclusion

In summary, we have demonstrated the structural changes and the specific roles of oxygen vacancies in PEC water oxidation process by constructing V_O-modified WO₃ photoanode. The WO₃-V_O exhibits a

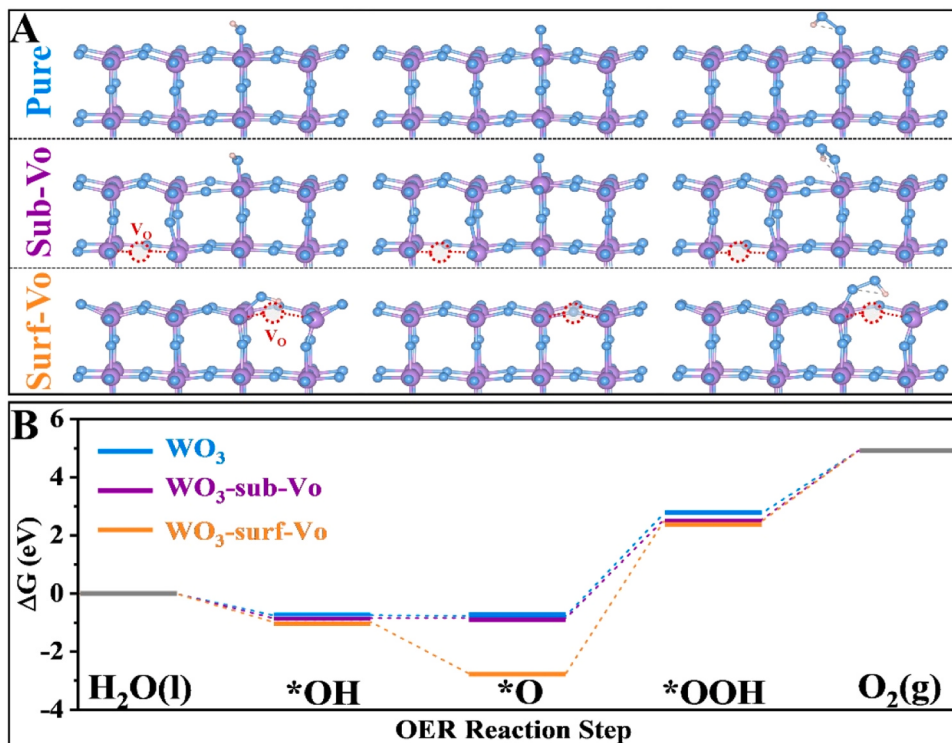


Fig. 4. (A) The optimized geometries of relevant species (*OH, *O and *OOH) during OER on WO₃ (010). (Blue: pure WO₃, purple: WO₃-sub-V_O, orange: WO₃-surf-V_O). (B) Reaction free-energy diagrams for OER on pure WO₃, WO₃-sub-V_O and WO₃-surf-V_O.

remarkable photocurrent density of 2.76 mA cm⁻² at 1.23 VRHE, which is 3 times higher than that of pristine WO₃ samples under AM 1.5 G solar irradiation. Relevant experiments and theoretical investigations have unveiled the crucial roles of surface and subsurface oxygen vacancies. Surface oxygen vacancies effectively restore the lattice structure by capturing oxygen atoms from adsorbed H₂O molecules, while subsurface oxygen vacancies significantly enhance charge transport and utilization, leading to improved PEC water oxidation activity. Importantly, we have also confirmed these phenomena and effects in the TiO₂ photoanode system. This research significantly advances the understanding of the function and mechanism of oxygen vacancy engineering in applications related to water oxidation.

CRediT authorship contribution statement

Lianglin Yan: Investigation, Formal analysis, Data curation, Writing - original draft. **Guojun Dong:** Methodology, Formal analysis, Investigation, Writing - original draft, Writing - review & editing, Funding acquisition. **Xiaojuan Huang:** Investigation. **Yun Zhang:** Supervision, Writing-review & editing. **Yingpu Bi:** Conceptualization, Supervision, Writing-review & editing, Project administration, Funding acquisition.

Declaration of Competing Interest

The authors declare that they have no known competing financial interests or personal relationships that could have appeared to influence the work reported in this paper.

Data availability

Data will be made available on request.

Acknowledgements

The work was supported by the National Natural Science Foundation

of China (22372181, 21832005, 22002175), The Science and Technology Planning Project of Chengguan District of Lanzhou City (2021RCCX0018), Science and Technology Planning Project of Gansu Province (23CXJA0004), Self-deployment Program of the Lanzhou Institute of Chemical Physics, CAS (2022000126).

Appendix A. Supporting information

Supplementary data associated with this article can be found in the online version at doi:10.1016/j.apcatb.2023.123682.

References

- [1] D.A. Tryk, A. Fujishima, K. Honda, Recent topics in photoelectrochemistry: achievements and future prospects, *Electrochim. Acta* 45 (2000) 2363–2376.
- [2] T. Hisatomi, J. Kubota, K. Domen, Recent advances in semiconductors for photocatalytic and photoelectrochemical water splitting, *Chem. Soc. Rev.* 43 (2014) 7520–7535.
- [3] A. Fujishima, K. Honda, Electrochemical photolysis of water at a semiconductor electrode, *Nature* 238 (1972) 37–38.
- [4] W. Bai, Y. Zhou, G. Peng, J. Wang, A. Li, P.F.X. Corvini, Engineering efficient hole transport layer Ferrihydrite-MXene on BiVO₄ photoanodes for photoelectrochemical water splitting: work function and conductivity regulated, *Appl. Catal. B Environ.* 315 (2022) 121606.
- [5] Z. Xie, D. Chen, J. Zhai, Y. Huang, H. Ji, Charge separation via synergy of homojunction and electrocatalyst in BiVO₄ for photoelectrochemical water splitting, *Appl. Catal. B Environ.* 334 (2023) 122865.
- [6] D. Chen, Z. Liu, S. Zhang, Enhanced PEC performance of hematite photoanode coupled with bimetallic oxyhydroxide NiFeOOH through a simple electroless method, *Appl. Catal. B Environ.* 265 (2019) 118580.
- [7] H. Kong, H. Yang, J.S. Park, W.S. Chae, H.Y. Kim, J. Park, J.H. Lee, S.Y. Choi, M. Park, H. Kim, Y. Song, H. Park, J. Yeo, Spatial control of oxygen vacancy concentration in monoclinic WO₃ photoanodes for enhanced solar water splitting, *Adv. Funct. Mater.* 32 (2022) 2204106.
- [8] Y. Kuang, Q. Jia, H. Nishiyama, T. Yamada, A. Kudo, K. Domen, A front-illuminated nanostructured transparent BiVO₄ photoanode for >2% efficient water splitting, *Adv. Energy Mater.* 6 (2016) 1501645.
- [9] H. Chai, L. Gao, P. Wang, F. Li, G. Hu, J. Jin, In₂S₃/F-Fe₂O₃ type-II heterojunction bonded by interfacial S-O for enhanced charge separation and transport in photoelectrochemical water oxidation, *Appl. Catal. B Environ.* 305 (2022) 121011.
- [10] T. Tran-Phu, Z. Fusco, I. Di Bernardo, J. Lipton-Duffin, C.Y. Toe, R. Daiyan, T. Gengenbach, C. Lin, R. Bo, H.T. Nguyen, G.M.J. Barca, T. Wu, H. Chen, R. Amal,

A. Tricoli, Understanding the role of vanadium vacancies in BiVO_4 for efficient photoelectrochemical water oxidation, *Chem. Mater.* 33 (2021) 3553–3565.

[11] Y. Li, Q. Mei, Z. Liu, X. Hu, Z. Zhou, J. Huang, B. Bai, H. Liu, F. Ding, Q. Wang, Fluorine-doped iron oxyhydroxide cocatalyst: promotion on the WO_3 photoanode conducted photoelectrochemical water splitting, *Appl. Catal. B Environ.* 304 (2022) 120995.

[12] H. Jun, B. Im, J.Y. Kim, Y.O. Im, J.W. Jang, E.S. Kim, J.Y. Kim, H.J. Kang, S. J. Hong, J.S. Lee, Photoelectrochemical water splitting over ordered honeycomb hematite electrodes stabilized by alumina shielding, *Energy Environ. Sci.* 5 (2012) 6375–6382.

[13] I.S. Cho, Z. Chen, A.J. Forman, D.R. Kim, P.M. Rao, T.F. Jaramillo, X. Zheng, Branched TiO_2 nanorods for photoelectrochemical hydrogen production, *Nano Lett.* 11 (2011) 4978–4984.

[14] B. Zhang, L. Wang, Y. Zhang, Y. Ding, Y. Bi, Ultrathin FeOOH nanolayers with abundant oxygen vacancies on BiVO_4 photoanodes for efficient water oxidation, *Angew. Chem. Int. Ed.* 57 (2018) 2248–2252.

[15] Y. Wang, W. Tian, C. Chen, W. Xu, L. Li, Tungsten trioxide nanostructures for photoelectrochemical water splitting: material engineering and charge carrier dynamic manipulation, *Adv. Funct. Mater.* 29 (2019) 1809036.

[16] J. Zheng, Y. Lyu, C. Xie, R. Wang, L. Tao, H. Wu, H. Zhou, S. Jiang, S. Wang, Defect-enhanced charge separation and transfer within protection layer/semiconductor structure of photoanodes, *Adv. Mater.* 30 (2018) 1801773.

[17] H. Zhang, P. Li, H. Zhou, J. Xu, Q. Jiang, J.H.L. Hadden, Y. Wang, M. Wang, S. Chen, F. Xie, D.J. Riley, Unravelling the synergy of oxygen vacancies and gold nanostars in hematite for the electrochemical and photoelectrochemical oxygen evolution reaction, *Nano Energy* 94 (2022) 106968.

[18] G. Dong, L. Yan, Y. Bi, Advanced oxygen evolution reaction catalysts for solar-driven photoelectrochemical water splitting, *J. Mater. Chem. A* 11 (2023) 3888–3903.

[19] C. Shao, A.S. Malik, J. Han, D. Li, M. Dupuis, X. Zong, C. Li, Oxygen vacancy engineering with flame heating approach towards enhanced photoelectrochemical water oxidation on WO_3 photoanode, *Nano Energy* 77 (2020) 105190.

[20] M. Kim, B. Lee, H. Ju, J.Y. Kim, J. Kim, S.W. Lee, Oxygen-vacancy-introduced $\text{BaSnO}_{3-\delta}$ photoanodes with tunable band structures for efficient solar-driven water splitting, *Adv. Mater.* 31 (2019) 1903316.

[21] S. Jin, X. Ma, J. Pan, C. Zhu, S. Saji, J. Hu, X. Xu, L. Sun, Z. Yin, Oxygen vacancies activating surface reactivity to favor charge separation and transfer in nanoporous BiVO_4 photoanodes, *Appl. Catal. B Environ.* 281 (2021) 119477.

[22] J. Zhang, X. Chang, C. Li, A. Li, S. Liu, T. Wang, J. Gong, WO_3 photoanodes with controllable bulk and surface oxygen vacancies for photoelectrochemical water oxidation, *J. Mater. Chem. A* 6 (2018) 3350–3354.

[23] S. Feng, T. Wang, B. Liu, C. Hu, L. Li, Z. Zhao, J. Gong, Enriched surface oxygen vacancies of photoanodes by photoetching with enhanced charge separation, *Angew. Chem. Int. Ed.* 59 (2020) 2044–2048.

[24] J.H. Kim, Y.J. Jang, J.H. Kim, J.-W. Jang, S.H. Choi, J.S. Lee, Defective ZnFe_2O_4 nanorods with oxygen vacancy for photoelectrochemical water splitting, *Nanoscale* 7 (2015) 19144–19151.

[25] J. Su, X. Feng, J.D. Sloppy, L. Guo, C.A. Grimes, Vertically aligned WO_3 nanowire arrays grown directly on transparent conducting oxide coated glass: synthesis and photoelectrochemical properties, *Nano Lett.* 11 (2011) 203–208.

[26] M.D. Segall, P.J.D. Lindan, M.J. Probert, C.J. Pickard, P.J. Hasnip, S.J. Clark, M. C. Payne, First-principles simulation: ideas, illustrations and the CASTEP code, *J. Phys. Condens. Matter* 14 (2002) 2717–2744.

[27] D. Srivastva, M. Menon, K. Cho, Nanoplasticity of single-wall carbon nanotubes under uniaxial compression, *Phys. Rev. Lett.* 83 (1999) 2973–2976.

[28] J.P. Perdew, K. Burke, M. Ernzerhof, Generalized gradient approximation made simple, *Phys. Rev. Lett.* 77 (1996) 3865–3868.

[29] J.P. Perdew, K. Burke, M. Ernzerhof, Generalized gradient approximation made simple, *Phys. Rev. Lett.* 78 (1997) 1396.

[30] M. Fang, Q. Cai, Q. Qin, W. Hong, W. Liu, Mo-doping induced crystal orientation reconstruction and oxygen vacancy on BiVO_4 homojunction for enhanced solar-driven water splitting, *Chem. Eng. J.* 421 (2021) 127796.

[31] L. Shi, W. Zhou, Z. Li, S. Koul, A. Kushima, Y. Yang, Periodically ordered nanoporous perovskite photoelectrode for efficient photoelectrochemical water splitting, *ACS Nano* 12 (2018) 6335–6342.

[32] X. Ma, J. Zhang, B. Wang, Q. Li, S. Chu, Hierarchical Cu_2O foam/g- C_3N_4 photocathode for photoelectrochemical hydrogen production, *Appl. Surf. Sci.* 427 (2018) 907–916.

[33] G. Wang, Y. Ling, H. Wang, X. Yang, C. Wang, J.Z. Zhang, Y. Li, Hydrogen-treated WO_3 nanoflakes show enhanced photostability, *Energy Environ. Sci.* 5 (2012) 6180–6187.

[34] J. Wang, Y. Zhang, T. Zhou, S. Chen, H. Zhu, J. Bai, J. Li, B. Zhou, Efficient WO_{3-x} nanoplates photoanode based on bidentate hydrogen bonds and thermal reduction of ethylene glycol, *Chem. Eng. J.* 404 (2021) 127089.

[35] J. Song, Z.F. Huang, L. Pan, J.J. Zou, X. Zhang, L. Wang, Oxygen-deficient tungsten oxide as versatile and efficient hydrogenation catalyst, *ACS Catal.* 5 (2015) 6594–6599.

[36] B. Lei, D. Xu, B. Wei, T. Xie, C. Xiao, W. Jin, L. Xu, In situ synthesis of $\alpha\text{-Fe}_2\text{O}_3/\text{Fe}_3\text{O}_4$ heterojunction photoanode via fast flame annealing for enhanced charge separation and water oxidation, *ACS Appl. Mater. Interfaces* 13 (2021) 4785–4795.

[37] K.A. Tsai, C.C. Lai, Y.H. Chen, I.C. Leu, J.C. Chang, C.Y. Kuo, S.W. Tseng, Y. Li, Y.-C. Pu, Exploring the impact of surface oxygen vacancies on charge carrier dynamics in BiVO_4 photoanodes through atmospheric pressure plasma jet post-treatment for efficiency improvement in photoelectrochemical water oxidation, *Appl. Catal. B Environ.* 341 (2024) 123288.

[38] F. Lei, Y. Sun, K. Liu, S. Gao, L. Liang, B. Pan, Y. Xie, Oxygen vacancies confined in ultrathin indium oxide porous sheets for promoted visible-light water splitting, *J. Am. Chem. Soc.* 136 (2014) 6826–6829.

[39] S. Corby, L. Francàs, A. Kafizas, J.R. Durrant, Determining the role of oxygen vacancies in the photoelectrocatalytic performance of WO_3 for water oxidation, *Chem. Sci.* 11 (2020) 2907–2914.

[40] K. Zhu, F. Shi, X. Zhu, W. Yang, The roles of oxygen vacancies in electrocatalytic oxygen evolution reaction, *Nano Energy* 73 (2020) 104761.

[41] S. Li, C. Liu, P. Chen, W. Lv, G. Liu, In-situ stabilizing surface oxygen vacancies of TiO_2 nanowire array photoelectrode by N-doped carbon dots for enhanced photoelectrocatalytic activities under visible light, *J. Catal.* 382 (2020) 212–227.

[42] F.Y. Xie, L. Gong, X. Liu, Y.T. Tao, W.H. Zhang, S.H. Chen, H. Meng, J. Chen, XPS studies on surface reduction of tungsten oxide nanowire film by Ar^+ bombardment, *J. Electron Spectrosc. Relat. Phenom.* 185 (2012) 112–118.

[43] G. Dong, X. Huang, Y. Bi, Anchoring black phosphorus quantum dots on Fe-doped $\text{W}_{18}\text{O}_{49}$ nanowires for efficient photocatalytic nitrogen fixation, *Angew. Chem. Int. Ed.* 61 (2022) e202204271.

[44] X. Wang, T. Wang, G. Si, Y. Li, S. Zhang, X. Deng, X. Xu, Oxygen vacancy defects engineering on Ce-doped $\alpha\text{-Fe}_2\text{O}_3$ gas sensor for reducing gases, *Sens. Actuators B Chem.* 302 (2020) 127165.

[45] Y. Zhang, Z. Xu, G. Li, X. Huang, W. Hao, Y. Bi, Direct observation of oxygen vacancy self-healing on TiO_2 photocatalysts for solar water splitting, *Angew. Chem. Int. Ed.* 58 (2019) 14229–14233.

[46] F. Bussolotti, L. Lozzi, M. Passacantando, S.L. Rosa, S. Santucci, L. Ottaviano, Surface electronic properties of polycrystalline WO_3 thin films: a study by core level and valence band photoemission, *Surf. Sci.* 538 (2003) 113–123.

[47] Y. Bai, H. Zhang, Q. Hu, Y. Zhou, B. Xiang, Tuning the kinetics of binder-free ammonium vanadate cathode via defect modulation for ultrafast rechargeable zinc ion batteries, *Nano Energy* 90 (2021) 106596.

[48] J. Wang, J. Liu, B. Zhang, H. Wan, Z. Li, X. Ji, K. Xu, C. Chen, D. Zha, L. Miao, J. Jiang, Synergistic effect of two actions sites on cobalt oxides towards electrochemical water-oxidation, *Nano Energy* 42 (2017) 98–105.

[49] I.C. Man, H.Y. Su, F. Calle-Vallejo, H.A. Hansen, J.I. Martínez, N.G. Inoglu, J. Kitchin, T.F. Jaramillo, J.K. Nørskov, J. Rossmeisl, Universality in oxygen evolution electrocatalysis on oxide surfaces, *ChemCatChem* 3 (2011) 1159–1165.

[50] R. Kishore, X. Cao, X. Zhang, A. Bieberle-Hütter, Electrochemical water oxidation on WO_3 surfaces: a density functional theory study, *Catal. Today* 321 (2019) 94–99.